Liver Tumor Segmentation Using Implicit Surface Evolution

Yrjö Häme
Helsinki, 6.7.2008

Abstract

A method for automatic liver tumor segmentation from computer tomography (CT) images is presented in this paper. Segmentation is an important operation before surgery planning, and automatic methods offer an alternative to laborious manual segmentation. In addition, segmentations of automatic methods are reproducible, so they can be reliably evaluated and they do not depend on the performer of the segmentation. In this work, the segmentation is performed in two stages. First a rough segmentation of tumors is obtained by simple thresholding and morphological operations. The second stage refines the rough segmentation result using fuzzy clustering and a geometric deformable model (GDM) that is fitted on the clustering result. The method was evaluated with data provided by Liver Tumor Segmentation Challenge 08, to which the method also participated. The data included 10 images from which 20 tumors were segmented. The method showed promising results.

Yrjö Häme is with the department of Biomedical Engineering and Computational Science of Helsinki University of Technology. Email: yrjo.hame@tkk.fi

1 Introduction

Important information of the condition and location of liver structures can be acquired by accurate image segmentation. Segmentation enables quantitative disease assessment and is an important step before surgery planning. Other purposes include research in pathology prediction by determining morphological and structural changes or deformations, multi-modality fusion and registration, navigation and image-guided surgery, 3D visualization and interactive segmentation. Manual segmentation is often laborious, inaccurate and the result varies strongly dependent on the observer. Manual segmentation is also not reliably reproducible. These shortcomings have created a demand for automatic and semi-automatic segmentation methods, which should be fast, accurate and robust. (See Pham et al [7]).

In the task of liver tumor segmentation from CT images, anatomical variance combined with limited resolution and random noise of the imaging method are common problems that require task-specific algorithms. Typically for medical images, the volumes are three-dimensional which complicates the task even further compared to simple two-dimensional images.

A novel method for automatic liver tumor segmentation from CT images is proposed in this paper. The segmentation is performed in two stages. First a rough segmentation of the tumors is obtained by simple thresholding and morphological operations. The second stage refines the rough segmentation result using a fuzzy clustering approach that incorporates a spatial smoothing term to the regular fuzzy c-means (FCM) clustering. The final tumor segmentation is obtained by fitting a geometric deformable model (GDM) on the membership function generated by the clustering. The approach of the refinement stage is similar to the one used for cortical reconstruction from magnetic resonance images by Han et al [1].

The method was evaluated using data provided by Liver Tumor Segmentation Challenge 08 (see http://lts08.bigr.nl/index.php), to which the method also participated. All parameter values used by the method are chosen to optimize performance for the training set of the evaluation data. After this introduction the second chapter describes the rough segmentation, followed by a description of the refinement stage in the third chapter. The fourth chapter presents results of the evaluation, and the fifth chapter concludes the document with a discussion.

2 Rough Segmentation

Starting with a raw CT image volume I (see fig. 1(a)), a constant with the value of 1000 is subtracted from the intensity values, resetting the scale so that voxels corresponding to air are assigned approximately an intensity value of -1000. The result of the subtraction is denoted by $I^{'}$. From $I^{'}$, three volumes are generated: the first one is a binary mask M_1 that is obtained by thresholding

$$M_1(\mathbf{x}) = \begin{cases} 1, \text{ when } a < I^{'}(\mathbf{x}) < b \\ 0, \text{ otherwise} \end{cases} \tag{1}$$

where $\mathbf{x} = [x_1, x_2, x_3]$ represents a single point in the image volume and the parameters are chosen as $a = -20$ and $b = 240$. From M_1, all holes with size of less than 10 are filled, and

the resulting mask covers all parts of the image $I^{'}$ with healthy liver tissue as well as all liver tumor tissue. The complement of M_1 is considered *background*.

The second volume is generated by filtering $I^{'}$ using a Gaussian filter with standard deviation of 1.0 in all three coordinate directions (x_1, x_2, x_3). The result is denoted by $I_g^{'}$. The third volume is generated by filtering $I^{'}$ one slice at a time using nonlinear diffusion (see Weickert [10]). Nonlinear diffusion smooths the image but preserves boundaries and produces piecewise constant regions, and it was used in a method for liver segmentation from CT images by Lamecker et al [3].

Let $I(\mathbf{x})$ be the original image, then the filtered image $F(\mathbf{x}, t)$ is obtained by solving the partial differential equation

$$\partial_t F = \text{div } g(|\nabla F_\sigma|^2)\nabla F) \tag{2}$$

when $F(\mathbf{x}, 0) = I(\mathbf{x})$ and F_σ is the result of Gaussian smoothing of F with standard deviation σ. The term $|\nabla F_\sigma|^2$ acts as an edge detector, and the diffusivity function $g(s)$ is defined as

$$g(s) := \begin{cases} 1 & (s \leq 0) \\ 1 - \exp(\frac{-3.315}{(s/\lambda)^4}) & (s > 0) \end{cases} \tag{3}$$

where λ controls how sensitive the smoothing is to intensity changes. In this work we used parameter values $\lambda = 3.0$, $\sigma = 1.4$ and $t = 100$. The result of the nonlinear diffusion filtering is denoted by $I_f^{'}$ (see fig. 1(b)).

Next, an intensity histogram is computed from a part of $I_f^{'}$, leaving the bottom 50 percent and the top 10 percent of the image slices out. For example, if $I_f^{'}$ has 200 image slices, the histogram is computed from the slices 101 to 180. The histogram is computed between intensity values 70 and 220 using histogram slot width of 1. The intensity with the highest corresponding value in the histogram is selected as the average intensity value for healthy liver tissue, denoted by α.

$I_f^{'}$ is then thresholded to create three binary masks M_2, M_3 and M_4 in the same fashion as above, using equation (1). The thresholds for M_2 are $a = 17$ and $b = \alpha$ and resulting in a mask that contains regions of tumors with low intensities and some of the healthy liver tissue (see fig. 1(c)). M_3 contains healthy liver tissue, and is created using thresholds $a = 0.82\alpha$ and $b = 1.25\alpha$ (see fig. 1(d)). M_4 is generated with thresholds $a = \alpha$ and $b = 240$, corresponding to tumors with high intensities and some of the healthy liver tissue (see fig. 1(e)).

Morphological opening is performed on M_3, using a spherical structuring element with the radius of 1, and from the result the largest connected component is selected using 6-connectivity, resulting in a binary object that is an initial estimate of the liver, denoted by $M_3^{'}$ (see fig. 1(f)). This object has typically many holes, particularly large at locations of tumors. Next we generate the filled mask M_a^{fill}, which is initialized as $M_3^{'}$. First advancing from the top of the image volume M_a^{fill} is filled one slice at a time using M_2, so that a slice k of M_a^{fill} (i.e. $M_a^{fill}(k)$) is changed to

$$M_a^{fill}(k) \leftarrow M_a^{fill}(k) \cup [M_2(k) \cap M_a^{fill}(k+1)]. \tag{4}$$

After this has been done for slice k, morphological closing is performed on it, using a disk-shaped structuring element with a radius of 6. Any remaining holes within slice k are filled,

and morphological opening is performed using the same structuring element as in closing. Then k is decreased by one and the same operation is repeated. After all the slices have been processed this way, the whole process is repeated starting from the bottom of the image volume, advancing in the direction of increasing k (using $M_a^{fill}(k-1)$ instead of $M_a^{fill}(k+1)$ in (4)). The result is a filled mask including all the healthy liver tissue and tumors with low intensities (see fig. 2(a)). In the same way, $M_b^{fill}(k)$ is generated for tumors with high intensities, but using M_4 instead of M_2 (see fig. 2(b)).

Finally, we extract the tumors from M_a^{fill} and M_b^{fill} by removing the healthy liver tissue and possible background regions from them. For this purpose $I_g^{'}$ is thresholded with the same parameter values as when creating M_3, $a = 0.82\alpha$ and $b = 1.25\alpha$, denoting the resulting mask by M_g. The removal is done in the same way for both masks:

$$M_a^{fill} \leftarrow M_a^{fill} \cap (M_1 \cup \neg M_g), \tag{5}$$

$$M_b^{fill} \leftarrow M_b^{fill} \cap (M_1 \cup \neg M_g), \tag{6}$$

(see fig. 2(c)). The resulting volumes are opened with spherical structuring element with radius of 4. From the resulting binary objects, the ones with size larger than 200 voxels are selected. These selected objects are the *tumor objects* for the refinement stage (see fig. 2(d)). However, it was noted that on rare occasions this approach was unable to detect a tumor at a desired location. For this reason, the set of tumor objects is supplemented by performing the tumor object extraction again, but this time using $M_3^{'}$ instead of M_g as the healthy liver tissue mask in equations (5) and (6). The resulting objects are added to the set of tumor objects only if they do not overlap with the existing tumor objects.

Each tumor object is dilated using a spherical structuring element with radius of 5. If the dilation leads to any part of the object expanding in background region ($\neg M_1$) or to overlap another tumor object, these parts are removed from the dilated object.

3 Refinement stage

3.1 Fuzzy clustering

The generated tumor objects are processed one at a time. The area covered by the dilated tumor object is extracted from $I^{'}$, and this part of the image is clustered in two classes with robust fuzzy C-means (RFCM) clustering as proposed by Pham [6]. RFCM includes a spatial smoothing term to reduce the effect of noise, compared to standard fuzzy c-means clustering.

When the number of classes is denoted by C, standard FCM minimizes the objective function J_{FCM} with respect to the membership values u and the centroids $\mathbf{v}$ (see Pham [6]):

$$J_{FCM} = \sum_{j \in \Omega} \sum_{k=1}^{C} u_{jk}^q ||y_j - v_k||^2 \tag{7}$$

where Ω is the set of voxel locations in the image volume, q is a parameter that controls the fuzziness of the classification and is constrained to be greater than one (if $q = 1$, FCM is equal to k-means clustering), u_{jk} is the membership value at voxel location j for class k so that $\sum_{k=1}^{C} u_{jk} = 1$, y_j is the image intensity at location j, and v_k is the centroid of class k. The objective function is minimized when high values are assigned to voxels with

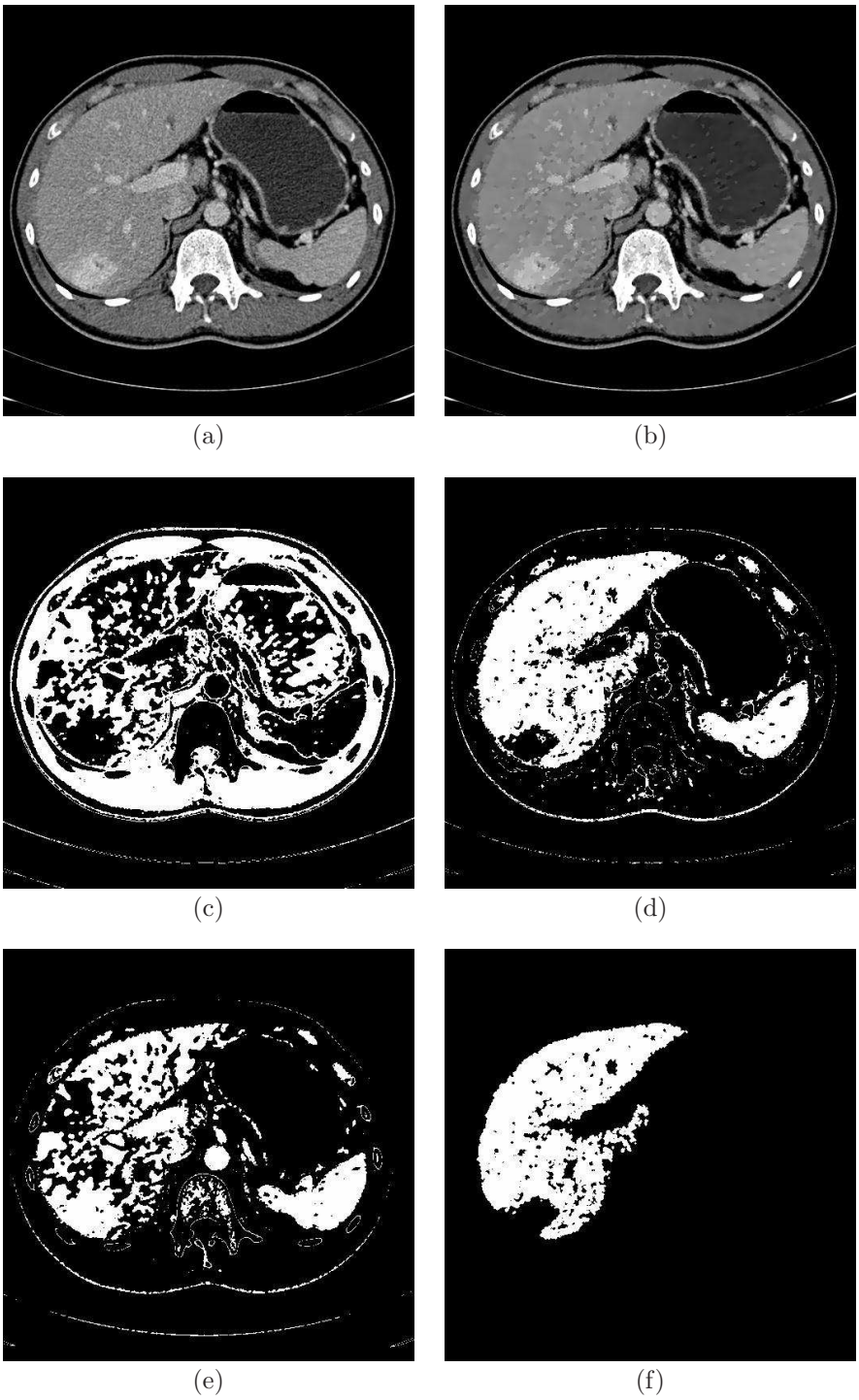

Figure 1 *(a) Original image, (b) image filtered with nonlinear diffusion, (c) mask M_2 (including tumor tissue with low intensities), (d) mask M_3 of healthy liver tissue, (e) mask M_4 (including tumor tissue with high intensities), (f) $M_3^{'}$, which is generated with morphological opening and extracting the largest connected component from M_3*

intensities close to the centroid of the particular class, and low values are assigned to voxels with intensities far from the centroid.

For spatial smoothing of the resulting membership functions, RFCM simply adds a second term to the objective function:

$$J_{RFCM} = \sum_{j\in\Omega}\sum_{k=1}^{C} u_{jk}^{q}||y_j - g_j v_k||^2 + \frac{\beta}{2}\sum_{j\in\Omega}\sum_{k=1}^{C} u_{jk}^{q}\sum_{l\in N_j}\sum_{m\neq k}^{C} u_{lm}^{q} \tag{8}$$

where N_j represents the set of first order neighbors of voxel j, and β is a weight constant that determines the smoothness between neighboring voxels in the resulting membership functions. In this implementation, RFCM was computed using a plug-in for MIPAV (see McAuliffe et al [4]), implemented by Pierre-Louis Bazin and Dzung L. Pham. The values used for the variables were $q = 2$, $C = 2$, $\beta = 0.1$ (this is the normalized value for β, which is multiplied by the square of intensity range in the image). The resulting membership functions for the two classes are denoted by μ_1 and μ_2, and the respective cluster centroids have the property $v_1 < v_2$.

For tumor objects generated from M_a^{fill}, μ_1 is used for directing the geometric deformable model, but only if $|v_1 - \alpha| > |v_2 - \alpha|$ (if this condition is not fulfilled, the tumor object is discarded). In the same way, for objects generated from M_b^{fill}, μ_2 is used, but only if $|v_1 - \alpha| < |v_2 - \alpha|$.

3.2 Geometric deformable model

In a standard geometric deformable model, the evolving curve or surface $\Gamma(t)$ is embedded as the *zero level set* of the higher-dimensional level set function $\phi(\mathbf{x}, t)$ (see Sethian et al [9]):

$$\Gamma(t) = \{\mathbf{x}|\phi(\mathbf{x}, t) = 0\} \tag{9}$$

The evolution is usually prescribed by a partial differential equation of the following form

$$\phi_t(\mathbf{x}, t) = F_{prop}(\mathbf{x})||\nabla\phi(\mathbf{x}, t)|| + F_{curv}(\mathbf{x})||\nabla\phi(\mathbf{x}, t)|| + \vec{F}_{adv}(\mathbf{x}) \cdot \nabla\phi(\mathbf{x}, t) \tag{10}$$

where F_{prop}, F_{curv} and $\vec{F}_{adv}$ are spatially varying speed terms and ϕ_t is the partial time derivative of ϕ. F_{prop} is an expansion or contraction speed in the normal direction, F_{curv} is the curvature term that depends on the intrinsic geometry of the surface and $\vec{F}_{adv}$ is the advection term, which represents an independent velocity field. (See Han et al [1,2]).

By convention, the level set function $\phi(\mathbf{x}, t)$ is initialized as a signed distance function to the initial surface $\Gamma(t = 0)$ (see Sethian et al [9])

$$\phi(\mathbf{x}, t = 0) = \pm d \tag{11}$$

where d is the distance from $\mathbf{x}$ to $\Gamma(t = 0)$, choosing negative values on the inside and positive on the outside of $\Gamma(t)$. If $\phi(\mathbf{x}, t)$ is a signed distance function, it also has a property $||\nabla\phi(\mathbf{x}, t)|| = 1$. After initialization, $\Gamma(t)$ is expressed as the zero level set of $\phi(\mathbf{x}, t)$ as presented in equation (9). Computing the signed distance function was done with the fast marching level set method (see Sethian et al [8]).

In this implementation of the geometric deformable model, the two speed terms F_{prop} and F_{curv} of equation (10) are used. F_{prop} is a signed pressure force computed from the fuzzy membership function μ and F_{curv} is proportional to the mean curvature $\kappa(\mathbf{x})$ of the surface. These choices form the evolution equation to

$$\phi_t(\mathbf{x}, t) = \omega_R R(\mathbf{x})||\nabla\phi(\mathbf{x}, t)|| + \omega_\kappa \kappa(\mathbf{x}, t)||\nabla\phi(\mathbf{x}, t)|| \tag{12}$$

where $R(\mathbf{x}) = 2\mu(\mathbf{x}) - 1$. ω_R and ω_κ are weights that cause the terms to be emphasized differently, chosen as $\omega_R = 1$ and $\omega_\kappa = -0.4$.

Following the definition of Osher et al [5], the normal $\vec{N}$ of the surface $\phi(\mathbf{x}, t)$ at point $\mathbf{x}$ is defined as

$$\vec{N} = \frac{\nabla\phi(\mathbf{x}, t)}{||\nabla\phi(\mathbf{x}, t)||} \tag{13}$$

and the mean curvature $\kappa(\mathbf{x})$ of the interface is the divergence of the normal

$$\kappa(\mathbf{x}) = \nabla \cdot \vec{N} = \nabla \cdot (\frac{\nabla\phi(\mathbf{x}, t)}{||\nabla\phi(\mathbf{x}, t)||}) \tag{14}$$

In this work, the numerical solution of 12 is obtained by simple upwind differencing (see Sethian et al [9]), also used by Han et al [1].
Topological flexibility of the geometric deformable models is usually considered as a great advantage but it also means that topological changes are difficult to prevent. This can be a significant problem when the initial topology of the surface is wished to be preserved. In this work, as a single connected binary object is desired as the result from each tumor object, we used a topology-preserving GDM proposed by Han et al [2]. This modification prevents sign changes at grid points of the level set function if the topology of the object is about to be altered. The final segmentation of the liver tumor is obtained after the GDM has reached a steady state by selecting all the points with negative values in $\phi(\mathbf{x}, t)$ as the segmented object.

4 Results

From the data of Liver Tumor Segmentation Challenge 08, 20 tumors in 10 images were used for evaluation. Of these data, 10 tumors from 4 images were used as training data for the method, and the remaining 10 tumors from 6 images as test data. Using reference segmentations created by an experienced radiologist and confirmed by another radiologist, five measures were computed from each segmentation generated by the proposed method: volumetric overlap error (%), relative absolute volume difference (%), average symmetric surface distance (mm), RMS symmetric surface distance (mm) and maximum symmetric surface distance (mm). These measures are described in more detail on the Liver Tumor Segmentation Challenge 08 website (see http://lts08.bigr.nl/).

The evaluation measures are presented in table 1 for both training and test data. For interpreting the results of the evaluation we categorize the results based on their overlap error. When the overlap error is smaller than 67%, a segmentation is considered *successful* and if the measure is smaller than 50%, a segmentation is considered *good*. Using this categorization, out of the total of 20 segmentations 17 are considered successful and 14 good. In table 2 the averages and standard deviations of the evaluation measures are listed for different categories.

From table 2 can be noted that for the *good* segmentations, the average measures have excellent values with small standard deviations. However, when including the remaining results the average values deteriorate substantially. This can be considered as evidence of good accuracy but lack of robustness of the method. Table 1 also shows, that the performance of the method varied largely between images. For example for the segmentations of image IMG04, which was part of the training data set and included 4 tumors, corresponding to

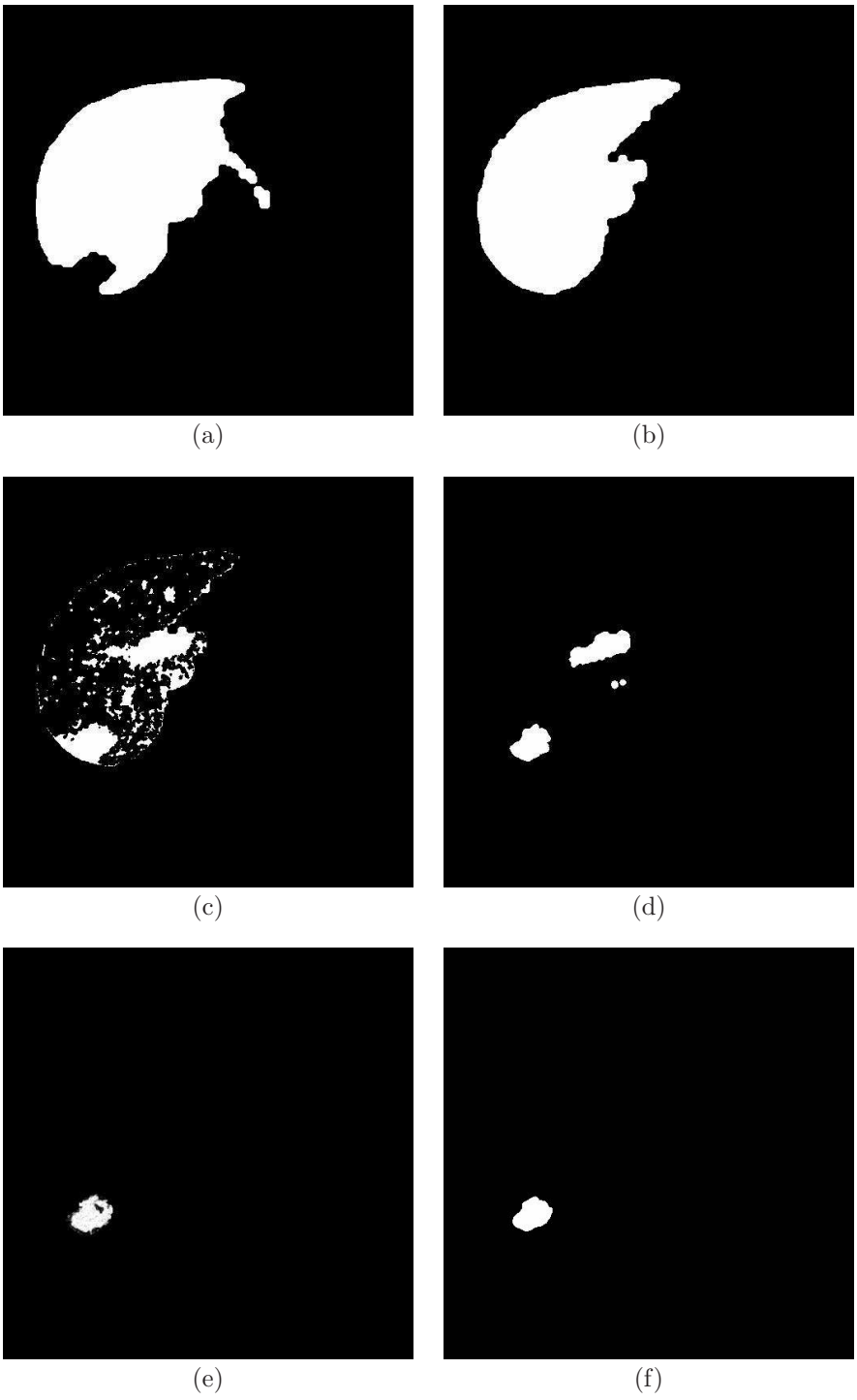

Figure 2 *Filled masks (a) M_a^{fill} and (b) M_b^{fill}, (c) M_b^{fill} with healthy liver tissue and background removed, (d) tumor candidate objects, (e) fuzzy segmentation class membership μ_2, (f) segmentation result*

40% of the training data, the method generated outstanding results for all segmentations. But for images such as IMG05 including 3 tumors in the test data, all the results were quite poor.

Table 1 *Results of the evaluation, where the segmentation of the proposed method was compared to a reference segmentation. The first ten cases were used as training data and last ten as test data.*

Tumor ID	Overlap Error (%)	Volume Difference (%)	Ave. Surf. Dist. (mm)	RMS Surf. Dist. (mm)	Max. Surf. Dist. (mm)
IMG01_L1	51.40	49.72	4.10	5.29	17.02
IMG01_L2	37.96	37.77	1.36	1.65	5.31
IMG02_L1	41.70	39.80	1.66	2.04	8.12
IMG02_L2	23.63	20.24	0.82	1.29	5.85
IMG02_L3	95.16	95.16	7.06	7.44	12.49
IMG03_L1	42.93	36.07	1.05	1.56	6.26
IMG04_L1	18.26	12.95	1.37	1.84	8.29
IMG04_L2	9.79	2.59	0.35	0.60	3.10
IMG04_L3	12.44	7.88	0.86	1.37	8.75
IMG04_L4	15.52	11.54	0.80	1.47	8.30
IMG05_L1	62.10	60.28	6.92	10.42	27.23
IMG05_L2	43.65	39.03	1.70	2.17	5.26
IMG05_L3	68.38	124.63	8.27	12.64	39.59
IMG06_L1	39.75	29.51	1.08	1.30	3.54
IMG06_L2	88.25	750.87	14.69	19.40	48.35
IMG07_L1	51.04	33.41	13.20	21.61	81.70
IMG07_L2	31.21	10.44	1.49	2.27	12.34
IMG08_L1	36.55	28.15	4.43	5.79	19.11
IMG09_L1	27.17	9.70	0.89	1.27	6.11
IMG10_L1	25.17	25.08	1.35	1.82	7.46

The most common problem in the segmentations was the rough segmentation result including parts of the image outside the liver. This occurred with tumors IMG05_03, IMG06_L2 (see figure 3(e)), IMG07_L1 (see figure 3(f)) and IMG08_01. Another notable problem was the rough segmentation result lacking a significant part of the tumor area, which happened with tumors IMG01_L1, IMG02_L3 and IMG05_L1 (see figure 3(d)). The fuzzy clustering and geometric deformable model worked expectedly in all cases. Examples of segmentation results are shown in figure 3.

The test data evaluation results were given points in Liver Tumor Segmentation Challenge 08, 100 points being the maximum for an exact match with the reference segmentation. For each evaluation metric a reference value from segmentation performed by independent users was assigned a score of 90. These reference values were

1. Volumetric overlap error [%] 12.94
2. Relative absolute volume difference [%] 9.64
3. Average symmetric surface distance [mm] 0.40
4. RMS symmetric surface distance [mm] 0.72
5. Maximum symmetric surface distance [mm] 4.0

Table 2 *Average values and standard deviations (average ± std) of evaluation measures in seven different categories: successful segmentations of training data (9 cases), all segmentations of training data (10 cases), successful segmentations of test data (8 cases), all segmentations of test data (10 cases), all good segmentations (14 cases), all successful segmentations (17 cases), and all segmentations (20 cases). Segmentations of tumors with IDs IMG02_L3, IMG05_L3 and IMG06_L1 were not included in the successful segmentations, since their overlap error was greater than 67%. In addition to these three, segmentations of tumors IMG01_L1, IMG05_L1 and IMG07_L1 were not included in the good segmentations, since their overlap error was greater than 50%.*

Data	Overlap Error (%)	Volume Difference (%)	Ave. Surf. Dist. (mm)	RMS Surf. Dist. (mm)	Max. Surf. Dist. (mm)
Training (s)	28.18 ± 15.41	24.28 ± 16.79	1.37 ± 1.09	1.90 ± 1.33	7.89 ± 3.89
Training (a)	34.88 ± 25.69	31.37 ± 27.44	1.94 ± 2.07	2.46 ± 2.16	8.35 ± 3.94
Test (s)	39.58 ± 12.51	29.45 ± 16.17	3.88 ± 4.31	5.83 ± 7.11	20.34 ± 26.07
Test (a)	47.33 ± 20.26	111.11 ± 227.22	5.40 ± 5.20	7.87 ± 7.76	25.07 ± 25.14
Good (70%)	28.98 ± 11.82	22.20 ± 13.04	1.37 ± 0.96	1.89 ± 1.2	7.7 ± 4.04
Succ. (85%)	33.55 ± 14.89	26.72 ± 16.20	2.55 ± 3.22	3.75 ± 5.20	13.75 ± 18.60
All (100%)	41.10 ± 23.40	71.24 ± 162.74	3.67 ± 4.24	5.16 ± 6.20	16.71 ± 19.50

The points were assigned by using linear interpolation or extrapolation between the two points specified above, with a minimum value of zero and rounded to the nearest integer. The points received from segmentations of the test data set were used to compare method performance in the competition. The method received an average of 48 points for the test data. Points for the training data segmentations were higher, with an average of 69 points. The points are listed in table 3.

From the table 3 can be seen that the method receives substantially lower points on average for surface distance measures than overlap error or volume difference. This is believed to be caused by the same problem as noted earlier: the method and more specifically the rough segmentation stage either misses a significant part of the tumor or includes parts of the image outside the liver. This way, the segmentation is relatively good for most part of the tumor, but the surface distances become large because of inaccuracies at a specific location.

Table 3 *Points of evaluation, when an average reference manual segmentation received 90 points. The points from the test data (last 10 cases) were used to compare the method to other participants in the Liver Tumor Segmentation Challenge 08.*

Tumor ID	Overlap Error	Volume Difference	Ave. Surf. Dist.	RMS Surf. Dist.	Max. Surf. Dist.	Total Score
IMG01_L1	60	48	0	27	57	38
IMG01_L2	71	61	66	77	87	72
IMG02_L1	68	59	59	72	80	68
IMG02_L2	82	79	80	82	85	82
IMG02_L3	26	1	0	0	69	19
IMG03_L1	67	63	74	78	84	73
IMG04_L1	86	87	66	74	79	78
IMG04_L2	92	97	91	92	92	93
IMG04_L3	90	92	79	81	78	84
IMG04_L4	88	88	80	80	79	83
Training data average	73	68	60	66	79	69
IMG05_L1	52	37	0	0	32	24
IMG05_L2	66	60	57	70	87	68
IMG05_L3	47	0	0	0	1	10
IMG06_L1	69	69	73	82	91	77
IMG06_L2	32	0	0	0	0	6
IMG07_L1	61	65	0	0	0	25
IMG07_L2	76	89	62	68	69	73
IMG08_L1	72	71	0	19	52	43
IMG09_L1	79	90	78	82	85	83
IMG10_L1	81	74	66	75	81	75
Test data average	64	56	34	40	50	48
Total average	68	62	47	53	64	59

5 Discussion

The proposed method produced very good results for a majority of the evaluation data. These were obtained when the rough segmentation stage was successful, indicating that the chosen approach for the refinement stage using fuzzy clustering and a geometric deformable model is able to generate reliably accurate results. However, the rough segmentation stage suffers currently from lack of robustness, which degrades the overall performance of the method. In the future we plan to combine the proposed tumor segmentation method with an accurate segmentation of the liver. This should improve the results dramatically for segmentations such as the ones that advanced to parts of the image outside the liver in the conducted evaluation.

The fuzzy clustering worked expectedly in all cases, but in the future it might be useful

to look into to the possibility of clustering data based on their absolute deviation from the average healthy tissue intensity, rather than using it directly on the intensity values. This way, tumors with low and high intensities would not be extracted separately, and a single tumor segmentation might include segments of the image with both low and high intensities.

Bibliography

[1] Han, X., Pham, D.L., Tosun, D., Rettmann, M.E., Xu, C., Prince, J.L., 2004. CRUISE: Cortical reconstruction using implicit surface evolution. NeuroImage 23, 997-1012.

[2] Han, X., Xu, C., Prince, J.L., 2003. A Topology Preserving Level Set Method for Geometric Deformable Models. IEEE Transactions on Pattern Analysis and Machine Intelligence, vol. 25, no. 6.

[3] Lamecker, H., Lange, T., Seebass, M., 2004. Segmentation of the Liver using a 3D Statistical Shape Model. ZIB-Report 04-09 (April 2004).

[4] McAuliffe M.J., Lalonde F.M., McGarry D., Gandler W., Csaky K., Trus B.L. Medical Image Processing, Analysis & Visualization In Clinical Research. IEEE Computer-based Medical Systems (CBMS) 2001, 381-386.

[5] Osher, S.J., Fedkiw, R., 2003. Level set methods and dynamic implicit surfaces. Springer-Verlag New York, Incorporated.

[6] Pham, D.L., 2001. Spatial Models for Fuzzy Clustering. Computer Vision and Image Understanding 84, 285-297.

[7] Pham, D.L., Xu, C., Prince, J.L., 2000. A survey of current methods in medical image segmentation. Annu. Rev. Biomed. Eng., vol. 2, pp. 315-337.

[8] Sethian, J.A., 1996. A fast marching level set method for monotonically advancing fronts. Proceedings of the National Academy of Sciences, vol. 93, 1591-1595.

[9] Sethian, J.A., 1999. Level set methods and fast marching methods: evolving interfaces in computational geometry, fluid mechanics, computer vision and materials science. Cambridge University Press, Cambridge, UK.

[10] Weickert, J., 1997. A review of nonlinear diffusion filtering. Lecture Notes in Computer Science, 1252:3-28.

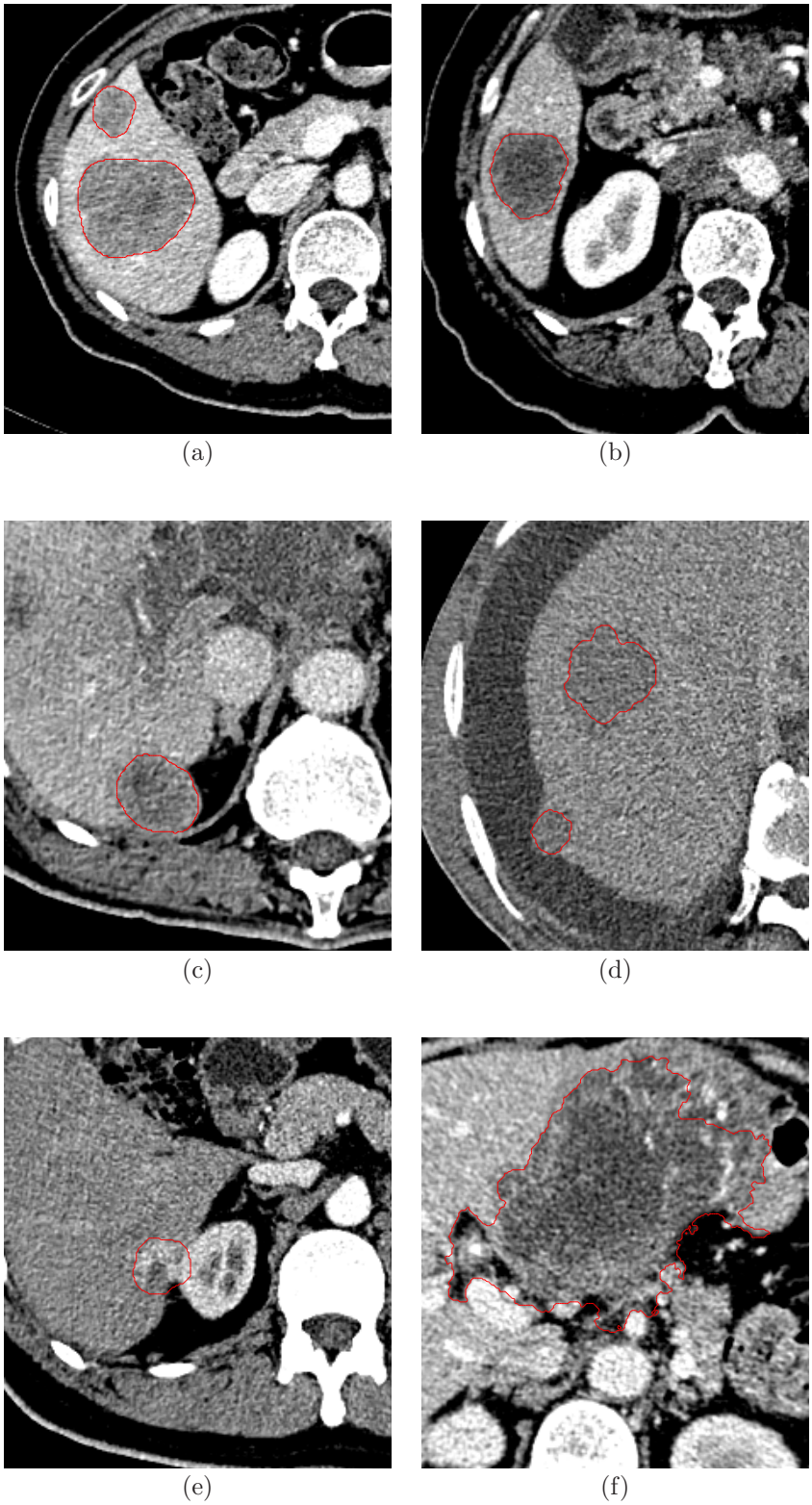

Figure 3 *Examples of segmentations overlaid on image slices (a) IMG04_L2 and IMG04_L3, (b) IMG10_L1, (c) IMG02_L2, (d) IMG05_L1 and IMG05_L2, (e) IMG06_L2 (with overflow to adjacent structure), (f) IMG07_L1 (with overflow to adjacent structure)*